Advanced Fault Location in MTDC Networks utilising Optically-Multiplexed Current Measurements and Machine Learning Approach

D. Tzelepis[a*], A. Dyśko[a], G. Fusiek[a], P. Niewczas[a], S. Mirsaeidi[b], C. Booth[a], X. Dong[b]

[a] *Department of Electrical and Electronic Engineering, University of Strathclyde, Glasgow, UK*
[b] *Department of Electrical Engineering, Tsinghua University, Beijing, P. R. China*

[*] *Technology & Innovation Centre, 99 George Street, G11RD, Glasgow, UK*
e-mail: dimitrios.tzelepis@strath.ac.uk
tel: +44(0)1414447268

Abstract

This paper presents a method for accurate fault localisation of DC-side faults in Voltage Source Converter (VSC) based Multi-Terminal Direct Current (MTDC) networks utilising optically-multiplexed DC current measurements sampled at 5 kHz, off-line continuous wavelet transform and machine learning approach. The technical feasibility of optically-based DC current measurements is evaluated through laboratory experiments using commercially available equipment. Simulation-based analysis through Matlab/Simulink® has been adopted to test the proposed fault location algorithm under different fault types and locations along a DC grid. Results revealed that the proposed fault location scheme can accurately calculate the location of a fault and successfully identify its type. The scheme has been also found to be effective for highly resistive fault with resistances of up to $500\ \Omega$. Further sensitivity analysis revealed that the proposed scheme is relatively robust to additive noise and synchronisation errors.

Keywords: Fault Location, Multi-Terminal Direct Current, Travelling Waves, Optical Sensors, Machine Learning, Pattern Recognition.

1. Introduction

High Voltage Direct Current (HVDC) power transmission are becoming increasingly competitive compared to high-voltage-alternating-current (HVAC) power transmission, especially for bulk power transmission over long distances. This is because of many commercial and technical advantages introduced by HVDC trasmission systems, utilising the most recently developed voltage source converters. Those advantages include bulk power transfer (notably from offshore wind [1]) over long distances [2], upgrading existing AC networks [3], interconnection of asynchronous grids and black start capability [4].

HVDC networks based on Modular Multilevel Converters (MMCs) is becoming progressively more favourable by the virtue of superior advantages, such as high efficiency, flexible control, scalability, and remarkable power quality with low harmonic content [5]. Further technical and economical improvements can arise by introducing MTDC systems which consist of more than two VSC stations and consequently the formation of a DC grid [6].

The majority of the existing operational and planned HVDC links are point-to-point with two points of connection with the AC networks. These connections are utilised for long distance power transmission within a country or for interconnection among different countries. At present, there is only one MTDC grid in operation located in Zhoushan, China, which was commissioned in 2013 [7]. However, with an increased penetration of renewable energy sources, balancing the supply and demand is likely to be one of the major challenges in future power systems [8]. Consequently, there is a growing need for meshed interconnections between countries in order to effectively share the available power capacity and thereby increase operational flexibility and security of supply. This has been raised as a major issue in Europe but also in Asia and United States of America. Before MTDC grids are widely adopted, it is essential to analyse the imposed potential challenges, like transient fault response [9], system integration, stability and power flow control [10].

After the occurrence of a feeder fault on a transmission system, protection systems are expected to minimise its detrimental effects, by initiating clearing actions such as selective tripping of circuit breakers. Following the successful fault clearance, the adjacent action is the accurate estimation of its location with regards to feeder's length. This is of major importance as it will enable faster system restoration, diminish the power outage time, and therefore enhance the overall reliability of the system. Therefore, this paper deals with the challenges involved in fault location of DC-side faults in MTDC systems.

The proposed scheme is based on a network of distributed current sensors installed at each feeder of an MTDC grid, and the subsequent travelling wave detection from DC current signatures. The accuracy of the proposed scheme is enhanced by the adoption of a machine learning approach, based on a pattern recognition scheme. The idea of distributed current sensors has been previously developed by the authors in [11] for protection applications in MTDC networks. The structure has been significantly expanded to be suitable for fault location applications in MTDC networks.

The remainder of the paper is organised as follows: Section 2 presents a literature review on the existing and proposed fault location techniques. Section 3 proposes and explains in detail the proposed fault location scheme. Section 4 presents the results of a thorough simulation-based evaluation of the proposed

scheme. Section 5 introduces the optical sensing technology and presents a series of experimental results, demonstrating the technical feasibility of optically-based DC current measurements. Finally, in Section 6 conclusions are drawn.

2. Fault Location in HVDC Systems

Travelling Waves (TWs) have been proposed as a very accurate solution for fault location both in AC and DC networks. According to the number of measurement points, TW-based fault location can be divided into single-ended and two-ended. The first one requires two consecutive waves to calculate the fault location. The two-ended methods requires the first waves, captured and time-stamped from both ends of a feeder.

The basic principle of single-end TWs alongside with two graph theory-based lemmas are utilised in [12] to locate the faults in MTDC networks. Nevertheless, high sampling frequency (1 MHz) is required, while detecting the first wavefront could be challenging [13]. A two-ended method based on Wavelet Transformation (WT) is utilised in [14] to locate faults in hybrid HVDC systems with both overhead lines (OHLs) and cables. The method requires voltages and capacitor current measurements, sampled at 2 MHz.

Another application of WT is utilised in [15] to accurately locate the faults in star-connected MTDC systems. The method necessitates measuring DC terminal currents and can eliminate the need of repeater station placement at the network junctions. However, both methods presented in [14] and [15] suffer from the need of time-synchronised measurements and high sampling frequency (2 MHz). Additionally, highly resistive faults have not been investigated thoroughly. In [16] a TW-based method is proposed by utilising voltage and current measurements from both ends of the faulted feeder. The method eliminates the need of both synchronised measurements and estimation of line parameters, and has been found to be accurate for both metallic and highly resistive faults (up to 500 Ω). However, there is a need for high sampling frequency (1 MHz). The method proposed in [17] eliminates the need to identify the precise arrival time of the surges. The proposed idea utilises the natural frequency of TWs (i.e. the dominant natural frequency in the spectrum analysis of TWs). For the execution of the algorithm, voltage and current measurements from one end (sampled at 100 kHz) are required. Even though the method has been found to be accurate, it has been tested only for highly resistive faults up tp 50 Ω.

Different from those methods which utilise TWs a few others can be found in the literature. In [18] the voltage distribution across the Burgeron line model is calculated in order to calculate the location of the fault. The sampling frequency required is only 6.4 kHz, while the method is accurate for long transmission lines and with highly resistive faults up to 500 Ω. However the method still requires time-synchronised

Table 1: Review of challenges related to fault location categories.

Fault location category	**Challenges**
Travelling waves	• Requirement of high sampling frequency. • Difficulties in detection of initial wave. • Speed of propagation should be known. • Impact of highly-resistive faults. • Need for time-synchronised measurements (two-ended method).
Reflectometry	• Need for external equipment. • High sampling frequency in the range of MHz to GHz. • Site visit to the feeder's terminal and assembly/disassembly of testing equipment.
Learning-based	• Training of the system is required. Since fault records are not always sufficient (or sometimes not available at all) the training is usually implemented by simulation-based iterative studies. This could raise concerns with regards to the reliability of the system training.

measurements. The article in [19] reviews the methods for diagnosing and locating faults in submarine power cables using the principles of reflectometry [20] , with case studies relevant to very long HVDC cables. Emphasis is put on the differences in the conditions and methods between locating a fault on a submarine cable from land cables, and the best practices for diagnosing and locating these types of faults are discussed. Even though that actual methodologies and test results are not presented thoroughly, it can be deduced that the need for external equipment and high sampling rates are drawbacks of these methods.

A special category of fault location practices (which is highly-related to the focus of this paper) incorporates the utilisation of learning-based approaches. Even though that such intelligent methods have been extensively used for localisation and classification of faults in AC networks [21, 22, 23, 24, 25], there is a limited number of publications which indicate their appropriateness for analysis of DC-side faults [13, 26, 27]. For example, based on post-fault voltage measurements sampled at 80 kHz, a method based on voltage similarity is proposed in [13]. The distance is calculated by calculating the Pearson coefficients with pre-simulated test patterns. Based on TWs and Support Vector Machine (SVM) another method is proposed in [26]. The method is single-ended and requires both current and voltage measurements. However the study cases consider fault resistance values up to 70 Ω, while the sampling frequency needs are not clearly stated.

Most of the fault location methods for HVDC lines can be classified in three major categories namely, 'TW-based', 'reflectometry-based' and 'learning-based'. A literature review of the methods falling under

the three aforementioned categories revealed that there is a wide selection of options which can accurately calculate the location of a fault. However, they are all accompanied by some technical challenges and barriers which are summarised in Table 1.

3. Proposed Fault Location Method

The fault location algorithm proposed in this paper is based on the availability and feasibility of optically-multiplexed current measurements (further analysis will be provided in Section 5). Such an experimental arrangement has been used previously in [11] for high-speed protection applications in MTDC networks. Therefore, the scheme has been significantly expanded to be suitable for fault location applications in MTDC networks.

The fault location technique consists of three main stages and utilises data buffers to store and process DC current records from all the available sensors along the faulted line. The flow chart of the fault location algorithm is depicted in Figure 6 and the stages are analysed in detail in the following subsections. It should be noted that prior to any signal analysis for the calculation of fault location, the optical signals are modulated and converted in DC current/voltage. This will be further analysed in Section 5.

3.1. Stage I: Fault Classification

Fault type is classified based on the post-fault DC current signatures. The possible types of fault include Pole-to-Pole Fault (PPF), Positive pole-to-Ground Fault (PGF) and Negative pole-to-Ground Fault (NGF). These have been assumed based on the relevant technical literature, addressing challenges arising from DC-side faults in VSC-based HVDC grids. The fault classification is implemented by utilising the positive and negative pole post-fault DC currents. For symmetric monopole systems, when a PPF occurs both positive and negative pole currents are expected to have fairly equal response in terms of amplitude. However, when a pole-to-ground fault occurs the current level of the faulted pole reaches significantly higher values (see Figure 1).

In order to justify the above, a PPF, a PGF and a NGF have been applied at 107 km on a 300 km HVDC transmission line. The resulting DC current traces are depicted in Figure 2. It is evident from the resulting DC current signatures that the fault can be classified by comparison between positive and negative pole currents. Since such measurements are not single values but they are rather a set of measurements over a short time window (e.g. around 5 ms), a comparison can be easier accelerated by calculating their area. The area of positive and negative pole currents are calculated by the integrals in equations 1 and 2 respectively.

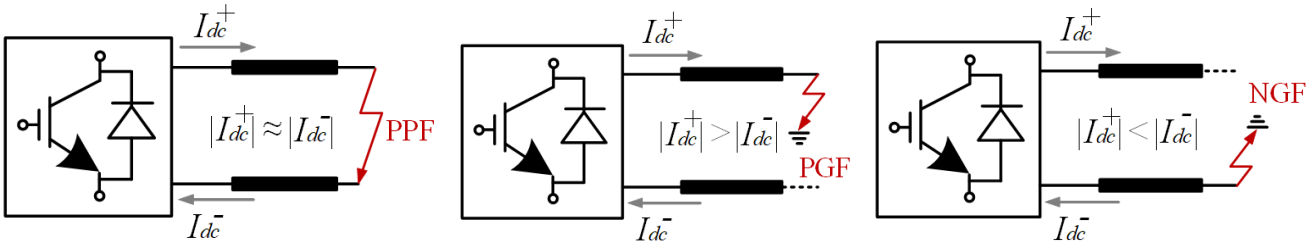

(a) Pole-to-pole fault (b) Positive pole-to-ground (c) Negative pole-to-ground

Figure 1: Illustration of different fault types for fault classification.

$$A_{Idc}^{+} = \int_{t_0}^{t_{end}} |i_{dc}^{+}| dt \tag{1}$$

$$A_{Idc}^{-} = \int_{t_0}^{t_{end}} |i_{dc}^{-}| dt \tag{2}$$

where, t_0 and t_{end} denote the starting and ending time of the available data windows, $|i_{dc}^{+}|$ represent $|i_{dc}^{-}|$ are the absolute value of positive and negative pole currents, respectively.

Since there is no formulation of the DC current traces, the trapezoidal method with unit spacing has been adopted for the calculation of their area. For the DC current traces depicted in Figure 2, the integrals of positive and negative pole currents have been calculated and listed in Table 2.

Table 2: Results of numerical integration of positive and negative pole currents.

Fault type	A_{Idc}^{+}	A_{Idc}^{-}
PPF	9,129,797.5	9,129,798,8
PGF	4,202,780.1	805,540.4
NGF	805,558.7	4,202,760.8

It is evident from Table 2 that in the case of a PPF, the area of both positive and negative pole currents are almost equal. On the contrary, for any other type of fault the area of the DC current for the faulted pole is significantly higher than the healthy one. In order to prevent any miscalculation due to induced noise and measurement uncertainties, the equality criterion for PPF has included a tolerance of $\pm 5\%$.

3.2. Stage II: Faulted Segment Identification

In this stage the closest sensors upstream and downstream to the fault are identified (i.e. the faulted segment is narrowed-down between two adjacent sensors). This is achieved by calculating the differential current I_{diff} for every pair of adjacent sensors, as presented in equation 3.

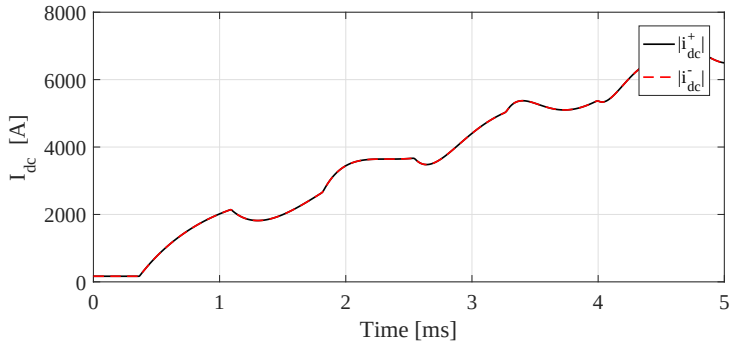

(a) Pole-to-pole fault

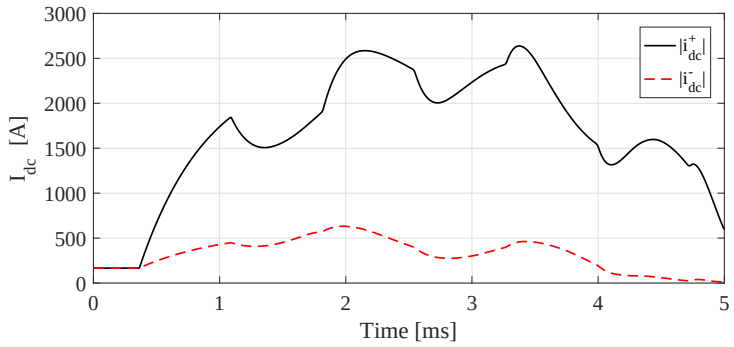

(b) Positive pole-to-ground

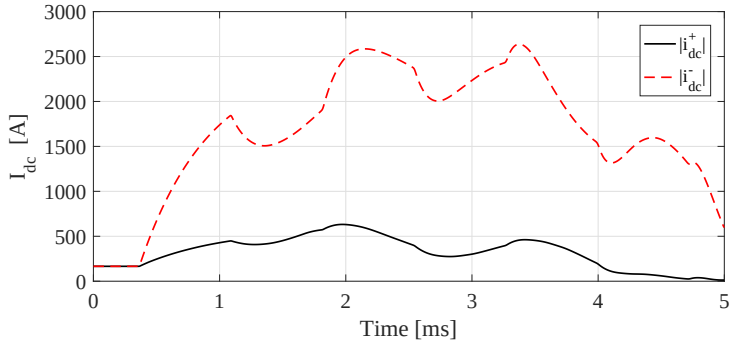

(c) Negative pole-to-ground

Figure 2: Simulation results (DC current signatures) of different fault types for fault classification.

$$I_{diff(s)} = i_{dc(s)} - i_{dc(s+1)} \tag{3}$$

where, s is the index of each sensor.

Considering a typical fault, as illustrated in Figure 3, it can be seen that the closest sensors to the fault are S_4 and S_5. The algorithm will start a routine to calculate the differential current for each pair of adjacent sensors. The resulting differential currents for this fault are indicated in Figure 4.

It is evident that the differential current $I_{diff(4)}$ (derived using measurements from sensors S_4 and S_5)

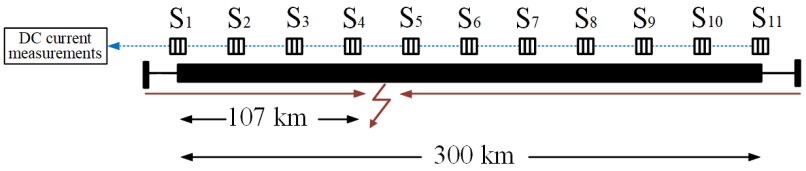

Figure 3: Fault occurrence on a 300 km transmission line incorporating distributed current sensors.

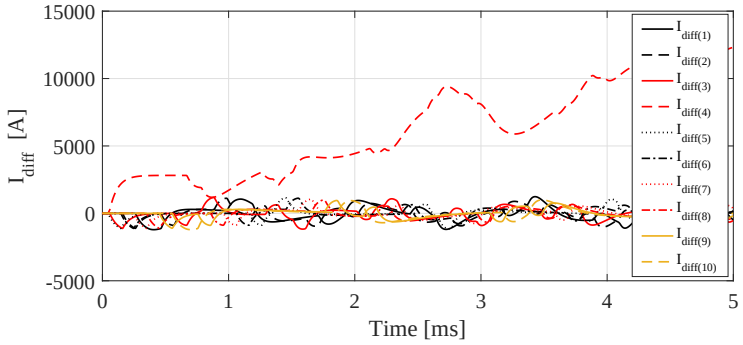

Figure 4: Differential currents derived for the fault case shown in Figure 3.

reaches significantly higher values than any other differential current. Consequently, a comparison among all the differential currents would provide the closest sensors to the fault. Instead of comparing the resulting differential currents with a pre-determined thresholds, their integral has been alternatively used according to equation 4.

$$A_{I_{diff(s)}} = \int_{t_0}^{t_{end}} |I_{diff(s)}| dt \tag{4}$$

For clarity of the above statement, the area of the differential currents presented in Figure 4 has been calculated according to equation 4. The resulting numerical calculations are presented in Table 3. It can be seen that the area of the differential current $I_{diff(4)}$ is significantly higher than the others, and hence, the faulted segment can be identified confidently.

Table 3: Numerical integration results of differential currents presented in Figure 4.

Sensors	$S_1 - S_2$	$S_2 - S_3$	$S_3 - S_4$	$S_4 - S_5$	$S_5 - S_6$	$S_6 - S_7$	$S_7 - S_8$	$S_8 - S_9$	$S_9 - S_{10}$	$S_{10} - S_{11}$
I_{diff}	$I_{diff(1)}$	$I_{diff(2)}$	$I_{diff(3)}$	$I_{diff(4)}$	$I_{diff(5)}$	$I_{diff(6)}$	$I_{diff(7)}$	$I_{diff(8)}$	$I_{diff(9)}$	$I_{diff(10)}$
$A_{I_{diff(s)}}$ $[10^6]$	1.12	1.01	0.96	15.46	0.51	0.65	0.71	0.73	0.72	0.76

Finally, this stage will generate two outputs; S_{up} and S_{dn}, which represent the index of the closest sensors upstream and downstream to the fault, respectively.

3.3. Stage III: Fault Location Calculation

The final stage of the proposed fault location algorithm is dedicated to the location of the fault. As the sensors closest to the fault have been identified in Stage II, captured post-fault data from all the sensors are utilised. In fact, the data are used to apply WT (WT is explained in detail in Appendix I) to locate the fault using two-ended technique between all the possible combinations upstream and downstream to the fault. Taking the example illustrated in Figure 5, it can be concluded that a two-ended TW-based fault location technique can be applied to every pairs of sensors, one at the upstream (i.e. sensors S_1 to S_4) and another at the downstream (i.e. sensors S_5 to S_{11}) of the fault.

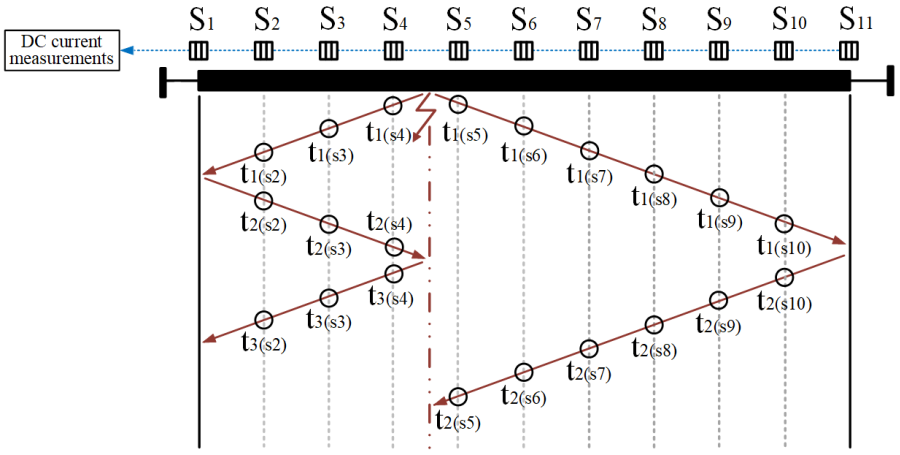

Figure 5: Bewley's Lattice diagram integrating distributed optical sensing network.

Consequently, the fault location results are calculated initially in the form of a matrix which, hereinafter, is referred to as *'Initial Fault Location Matrix'* (IFLM), and its dimensions are determined by the faulted segment. Considering the fault case illustrated in Figure 5, the nearest sensors to the fault are S_4 and S_5. This will result in an IFLM with number of rows and columns being equal to the number of sensors upstream and downstream to the fault, respectively, as illustrated in Table 4.

Table 4: IFLM for a fault occurring between sensors S_4 and S_5 (fault case depicted in Figure 5).

	$\mathbf{S_5}$	$\mathbf{S_6}$	$\mathbf{S_7}$	$\mathbf{S_8}$	$\mathbf{S_9}$	$\mathbf{S_{10}}$	$\mathbf{S_{11}}$
$\mathbf{S_1}$	$D_{f(1:5)}$	$D_{f(1:6)}$	$D_{f(1:7)}$	$D_{f(1:8)}$	$D_{f(1:9)}$	$D_{f(1:10)}$	$D_{f(1:11)}$
$\mathbf{S_2}$	$D_{f(2:5)}$	$D_{f(2:6)}$	$D_{f(2:7)}$	$D_{f(2:8)}$	$D_{f(2:9)}$	$D_{f(2:10)}$	$D_{f(2:11)}$
$\mathbf{S_3}$	$D_{f(3:5)}$	$D_{f(3:6)}$	$D_{f(3:7)}$	$D_{f(3:8)}$	$D_{f(3:9)}$	$D_{f(3:10)}$	$D_{f(3:11)}$
$\mathbf{S_4}$	$D_{f(4:5)}$	$D_{f(4:6)}$	$D_{f(4:7)}$	$D_{f(4:8)}$	$D_{f(4:9)}$	$D_{f(4:10)}$	$D_{f(4:11)}$

The cell contents of such a table correspond to the fault location as calculated by the two-ended TW-based between the sensors (for example, the value of $D_{f(1:5)}$ corresponds to the fault location as calculated

between sensors S_1 and S_5).

The generic two-end method for locating faults is presented in equation 5:

$$d_f = \frac{1}{2}(L + dtV) \tag{5}$$

where, d_f is the fault distance; L is the total length of the line; dt the time difference of the arrival of waves; and, V the propagation velocity.

Considering a fault between sensors S_{up} and S_{dn} as illustrated in Figure 5 (S_4 and S_5 at this case), the waves are detected at the time instances $t_{1(S_{up})}$ and $t_{1(S_{dn})}$, respectively ($t_{1(S4)}$ and $t_{1(S5)}$ at this case). Hence, the location of fault between sensors S_{up} and S_{dn} can be calculated using equation 6:

$$d_{f_{(s_{up}-s_{dn})}} = \frac{1}{2}\left(\frac{L}{n_s - 1} + dt_{(S_{up},S_{dn})}\, V\right) \tag{6}$$

where, $d_{f_{(s_{up}-s_{dn})}}$ is the distance of the fault between sensors S_{up} and S_{dn}, $dt_{(S_{up},S_{dn})}$ is the time difference between arrival of the two waves at sensors S_{up}, and S_{dn} and n_s is the total number of sensors installed on the transmission line.

The exact fault location taking as reference the left side of the line is calcualted by equation 7 (when fault is closest to the sensor S_{up}), and equation 8 (when fault is closest to the sensor S_{dn}).

$$D_{f(up:dn)} = \frac{L}{n_s - 1}\,(S_{up} - 1) + d_{f_{(s_{up}-s_{dn})}} \tag{7}$$

$$D_{f(dn:up)} = \frac{L}{n_s - 1}\,(S_{dn} - 1) - d_{f_{(s_{dn}-s_{up})}} \tag{8}$$

Equations 7 and 8 are used for all possible pairs of sensors, one at the upstream and another at the downstream of the fault in order to generate the fault matrix, as shown in Table 4.

Due to the reduced sampling frequency, (i.e. 5 kHz) it is expected that the fault location values contained in IFLM will have increased errors. One solution to reduce the error is the utilisation of much higher sampling frequency in the range of MHz. However, for the proposed distributed current sensing scheme this would require an extreme upgrade to the equipment accompanied with increased complexity in signal processing and cost. Therefore, on an attempt to reduce the potential fault location errors resulting from low sampling frequency, while maintaining the cost to the barely minimum, a machine learning approach is introduced in Stage III (see Figure 6 steps c to e).

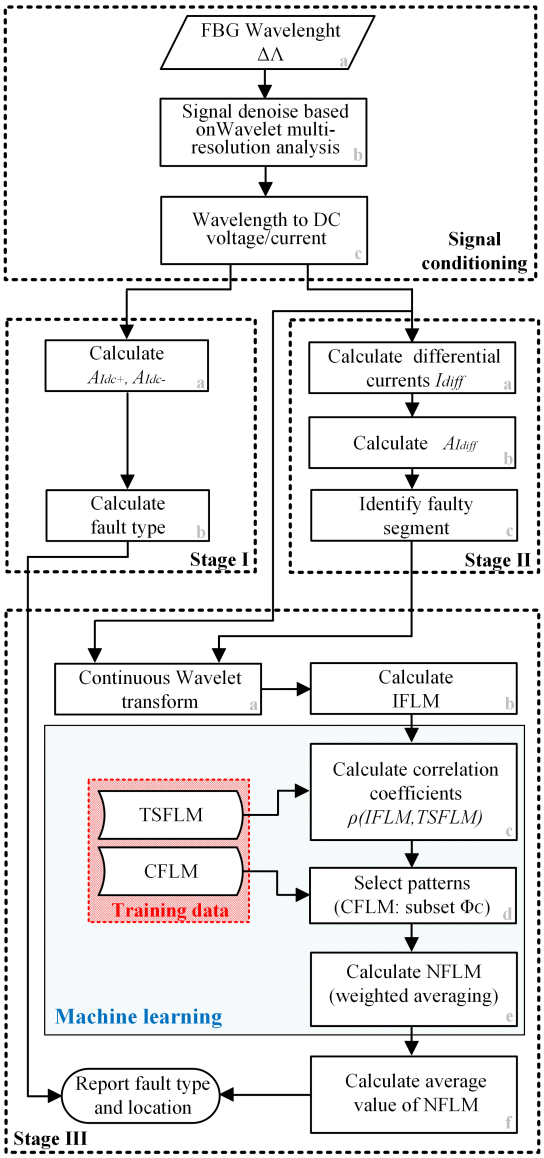

Figure 6: High level fault location algorithm flow chart.

The machine learning approach requires training samples, which are pre-simulated faults along a transmission line. For each training sample, (i.e. fault case) a *'Training Sample Fault Location Matrix'* (TSFLM) and a *'Compensating Fault Location Matrix'* (CFLM) is calculated. The former is the same as described before (i.e. IFLM) and shown in Table 4 (i.e. table with fault location calculated for each measurement from different sensors sampled at 5 kHz). The latter is a matrix which aims to compensate for errors calculated and included in the TSFLM. Specifically, the CFLM values are calculated having the knowledge fault location, as presented in equation 9. Therefore, when CFLM is multiplied by the TSFLM, (via element-wise multiplication) the resulting table is expected to have zero error.

$$CFLM = \frac{\text{Known fault location}}{TSFLM} \tag{9}$$

Below is a numerical example taking as guiding case the fault presented in Figure 5 and the fault location assumed to be known (i.e. 107 km).

$$\underbrace{\begin{bmatrix} 1.0405 & 0.9900 & 1.0030 & 0.9460 & 0.9762 & 1.0570 & 0.9788 \\ 1.0632 & 0.9690 & 1.0505 & 1.0283 & 1.0070 & 1.0533 & 0.9852 \\ 0.9769 & 0.9955 & 0.9967 & 1.0376 & 1.0379 & 1.0477 & 1.0617 \\ 1.0266 & 0.9904 & 0.9486 & 0.9864 & 0.9368 & 1.0439 & 0.9389 \end{bmatrix}}_{CFLM} = \underbrace{\begin{bmatrix} 102.84 & 108.08 & 106.68 & 113.11 & 109.60 & 101.23 & 109.31 \\ 100.64 & 110.43 & 101.86 & 104.05 & 106.26 & 101.59 & 108.61 \\ 109.53 & 107.49 & 107.36 & 103.13 & 103.09 & 102.13 & 100.78 \\ 104.23 & 108.04 & 112.79 & 108.47 & 114.22 & 102.50 & 113.97 \end{bmatrix}^{-1}}_{TSFLM} \cdot 107$$

When a fault with unknown fault location has occurred, as described before, the segment has been identified and the IFLM has been generated. A routine will then be initiated and will calculate the correlation coefficients of the IFLM (with the unknown fault location) and the TSFLM of the training samples.

The generic expression of Pearson's correlation coefficients of two variables K and U is expressed through equation 10:

$$\rho(K,U) = \frac{1}{N-1} \sum_{j=1}^{N} \left(\frac{K_j - \mu_K}{\sigma_K} \right) \left(\frac{U_j - \mu_U}{\sigma_U} \right) \tag{10}$$

where, $\rho(K,U)$ is the Pearson correlation coefcient of signals K and U (with $\rho(K,U) \in$ [-1,+1]), K and U are the variables (simulated and sampled Fault Matrices at this case), N denotes the scalar observations, μ_K, σ_K, μ_U and σ_U are the mean and standard deviation of K and U respectively.

Taking into account that K and U correspond to IFLM (case with unknown fault location) and TSFLM (training samples with known fault location) respectively, equation 10 is rewritten as follows:

$$\rho(IFLM, TSFLM) = \frac{1}{N-1} \sum_{j=1}^{N} \left(\frac{IFLM_j - \mu_{(IFLM)}}{\sigma_{(IFLM)}} \right) \left(\frac{TSFLM_j - \mu_{(TSFLM)}}{\sigma_{(TSFLM)}} \right) \tag{11}$$

The correlation coefficients is used like a measure of similarity and will provide the ability to match a simulated case (with unknown fault location) with any of the training samples (where the fault location is known and its CFLM can be used). Values of -1 and +1 impose a perfect negative and positive linear correlation, respectively, while the value of zero indicates no correlation at all. If two matrices are alike high values close to +1 are expected.

When there is a match between two matrices then the CFLM from the corresponding training sample is selected. The matching procedure is achieved by comparing the resulting similarity $\rho(IFLM, TSFLM)$ with a predefined threshold. For the cases presented in this paper, those which have more than 90 $\%$ similarity are selected, forming the sub-set Φ_C.

The sub-set Φ_C is used to produce a new matrix termed here are as *'Normalised Fault location Matrix'* (NFLM) and is calculated according to equation 12.

$$NFLM = IFLM \times \underbrace{\frac{\sum\limits_{z\in\Phi_C} CFLM(z)\, e^{-(1-\rho(IFLM,TSFLM))^2}}{\sum\limits_{z\in\Phi_C} e^{-(1-\rho(IFLM,TSFLM))^2}}}_{\text{weighted averaging function}} \tag{12}$$

The NFLM contain values of fault location which are normalised closer to the actual fault location, and hence, the errors are expected to be remarkably lower. This is established by multiplying the IFLM by a weighted averaging function. Such a function is utilised to influence on the result of different matching patterns (i.e. sub-set Φ_C) and apply different 'weight'. Greater influence is expected to be applied at zero metric distance (i.e. when similarity $\rho(IFLM, TSFLM) = 1$) and the function should fade out as the distance increases according to the chosen kernel. For the studies in this paper, the averaging function has been built upon exponential kernels [28, 29]. It should be noted that the matrix operations (i.e. multiplication, division, etc.) in equation 12 has been carried out in a element-wise manner.

Finally, the calculated fault distance $C.F_d$ is estimated by averaging the NFLM, as shown in equation 13:

$$C.F_d = \overline{NFLM} \tag{13}$$

The calculated values of fault location included in NFLM, are expected to deviate from the actual fault location. However, it is difficult to predict or calculate which values of NFL are closer or further to the actual fault location. Consequently, it is cumbersome and dicey to make a decision or conclude the fault distance from a single value. This is especially risky when a set of values might contain outliers (i.e. observation points that are much more distant from other observations). In order to address such challenge, and get a representative sample taking into account the contribution of all the observation points in the group, the averaging function has been utilised.

It should be highlighted that any concerns regarding the complexity of any machine learning approach may be eliminated, when the application is related to fault location. This is due to the fact that fault location is mostly related with accuracy, and there is always a wide time margin for off-line calculations.

4. Simulation-based Analysis

4.1. MTDC Network

A five-terminal HVDC has been utilised in the simulation case studies as illustrated in Fig. 7, which have been adopted according to the Twenties Project case study on DC grids [30]. The MTDC network is

equipped with five MMCs operating at ± 400 kV (symmetric monopole) and current limiting inductors at each transmission line end. The characteristics of the AC and DC networks are described in detail in Table 5.

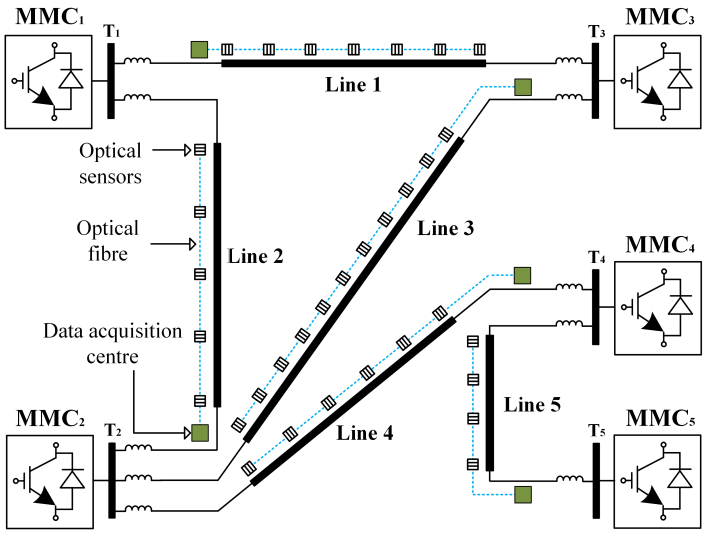

Figure 7: Five-terminal case study HVDC network.

Optical current sensors have been installed on each transmission line current every 30 kilometres (including the terminals, where the measurement and fault location station is located). Therefore, for lines 1 to 5, seven, five, eleven, six and four DC current sensors have been utilised, respectively. The fault location results are reported taking as a reference point the measurements and fault location station.

Table 5: DC and AC Network Parameters.

Parameter	**Value**
DC voltage [kV]	$\pm$ 400
DC inductor [mH]	150
Line resistance [Ω/km]	0.015
Line inductance [mH/km]	0.96
Line capacitance [μF/km]	0.012
Line lengths (1 to 5) [km]	180, 120, 300, 150, 90
AC frequency [Hz]	50
AC short circuit level [GVA]	40
AC voltage [kV]	400

It should be noted that in order to emulate any measurement errors originating from induced noise, external disturbances and measurements uncertainties, the measurements have been contaminated with artificial, random white noise.

The MTDC network including transmission lines, converters, current limiting inductors and network of optical current sensors is identical to the one used in [11] for protection studies.

4.2. Modular Multi-level Converters

The models of power converters utilised in these studies are based on 401-level Type 4 half bridge (HB) MMCs which have been developed according to guidelines and approaches described in [31, 1]. Such representation has been validated against fully detailed models and has been demonstrated to accurately represent the converter behaviour during steady-state, transient and fault conditions, while remaining numerically stable and computationally efficient. Figure 8 illustrates the equivalent of Type 4 for one phase.

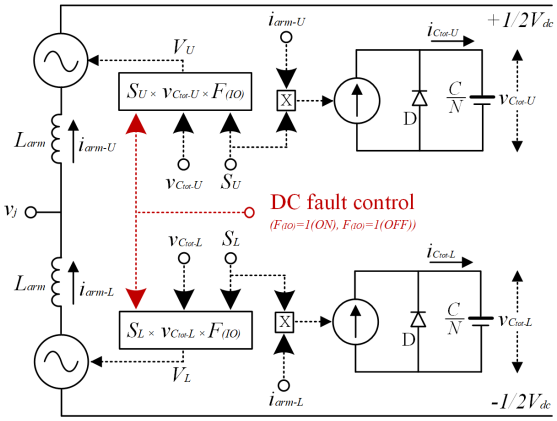

Figure 8: Equivalent of the MMC Type 4 Model.

Table 6: DC and AC Network Parameters.

Parameter	**Value**
DC voltage [kV]	$\pm$ 400
AC voltage [kV]	400
MMC levels	401
MMC arm inductance [p.u.]	0.1
MMC equivalent arm capacitance [μF]	20.84

The converter response is achieved through controlled voltage and current sources. A fault controller is also included which bypasses the sub-modules when the maximum current of the IGBTs is exceeded. In this case, the converter behaves like an uncontrolled rectifier. Due to imbalanced voltage conditions, circulating currents are generated inside each MMC which increase current stress, introduce current distortion (arm currents), and produce additional conduction losses. To eliminate such currents, a Proportional Resonant,

Circulating Current Suppression Controller (PR-CCSC), as described in [32], has been integrated into the control system.

4.3. Obtaining Training Data

The training fault patterns, have been generated by applying a series of PPF, PGFs and NGFs at all different transmission lines of the network depicted in Figure 5. The faults have been triggered at various distances along the feeders and for a wide range of fault resistances R_f from $0\ \Omega$ to $500\ \Omega$.

It should be noted that when adopting learning-based methods for power system studies, the generation of the training data is considered one of the main challenges (this is also highlighted in Table 1). In the case of an actual field project, the procedure of obtaining training data would be similar (i.e. development of a system model and then implementation of fault studies). However, the modelling of the system would have to be carried out considering the actual systems specification (i.e. voltage level, line parameters, etc.). Additional training data could be obtained from records of actual faults (with known location) during the commissioning of line fault-location and protection systems [15].

4.4. Fault Location Results

PPFs and PGFs have been triggered at all DC lines and at various locations. The reported fault location errors have been calculated according to Equation 14.

$$error\ \% = \frac{C.F_d - A.F_d}{L_{FL}} \cdot 100\% \tag{14}$$

where, $C.F_d$ and $A.F_d$ represented the calculated and actual fault distance; and L_{FL} denotes the length of the faulted line.

Tables 7, 8 and 9 illustrate the fault classification, segment identification and location results for PPFs, PGFs and NGFs, respectively. For such studies, Haar mother wavelet has been utilised with a scaling factor of $\alpha = 10$. It should be noted that 5 ms is considered for the available data window of measurements(predicted time window for the available post-fault measurements). This is due to the fact that protection systems are expected to clear any DC-side faults around this time slot (including detection and physical isolation).

Satisfactory results have been achieved for both type of faults at all locations. In all cases, the type of fault has been classified correctly while the segment of the fault has been identified precisely. The minimum, maximum and average error for PPFs reached values of $0.0000\ \%$, $0.1997\ \%$ and $0.0797\ \%$, respectively.

For PGFs those errors correspond to $0.0100\ \%$, $0.2310\ \%$ and $0.0987\ \%$ and for NGF to $0.0012\ \%$, $0.8860\ \%$ and $0.1357\ \%$, respectively.

Table 7: Fault classification, segment identification and location results for pole-to-pole faults.

Line	Fault distance [km]	Reported fault type	Reported sensor S_{up}	Reported sensor S_{dn}	Reported fault location [km]	Fault location error [%]
1	31	PPF	2	3	31.1343	0.0746
1	90	PPF	3	4	89.9737	-0.146
1	127	PPF	5	6	127.0099	0.0055
1	132	PPF	5	6	131.8678	-0.0735
1	142	PPF	5	6	141.7413	-0.1437
1	157	PPF	6	7	156.8166	-0.1019
2	16	PPF	1	2	15.8657	-0.1119
2	30	PPF	1	2	29.8878	-0.0935
2	47	PPF	2	3	47.1322	0.1102
2	97	PPF	4	5	97.1325	0.1104
2	112	PPF	4	5	111.8639	0.1134
3	20	PPF	1	2	20.5992	0.1997
3	58	PPF	2	3	58.0926	0.0309
3	128	PPF	5	6	128.0734	0.0245
3	176	PPF	6	7	176.1322	0.0441
3	212	PPF	8	9	212.1343	0.0448
3	296	PPF	10	11	296.0000	0.0000
4	23	PPF	1	2	23.0057	0.0038
4	38	PPF	2	3	38.0886	0.0591
4	75	PPF	3	4	75.2296	0.1531
4	97	PPF	4	5	97.2136	0.1424
4	134	PPF	5	6	134.1343	0.0895
5	8	PPF	1	2	7.9578	-0.0469
5	30	PPF	1	2	30.0549	0.0610
5	45	PPF	2	3	45.0149	0.0166
5	82	PPF	3	4	82.0397	0.0441

Table 8: Fault classification, segment identification and location results for positive pole-to-ground faults.

Line	Fault distance [km]	Reported fault type	Reported sensor S_{up}	Reported sensor S_{dn}	Reported fault location [km]	Fault location error [%]
1	23	PGF	1	2	23.1560	0.0867
1	53	PGF	2	3	53.2420	0.1345
1	107	PGF	4	5	107.1322	0.0735
1	112	PGF	4	5	112.1592	0.0885
1	157	PGF	6	7	156.8166	-0.1019
2	8	PGF	1	2	7.7907	-0.1744
2	43	PGF	2	3	43.1343	0.1119
2	60	PGF	2	3	59.9610	-0.0325
2	73	PGF	3	4	72.8678	-0.1102
2	112	PGF	4	5	111.8639	-0.1134
3	35	PGF	2	3	35.1343	0.0448
3	84	PGF	3	4	83.6381	-0.1206
3	179	PGF	6	7	179.0300	0.0100
3	198	PGF	7	8	197.6388	-0.1204
3	220	PGF	8	9	220.4008	0.1336
3	267	PGF	9	10	267.0690	0.0230
3	280	PGF	10	11	279.3070	-0.2310
4	18	PGF	1	2	18.1322	0.0881
4	38	PGF	2	3	38.0886	0.0591
4	75	PGF	3	4	75.2296	0.1531
4	102	PGF	4	5	102.1343	0.0895
4	142	PGF	5	6	141.7071	-0.1953
5	17	PGF	1	2	17.1322	0.1469
5	30	PGF	1	2	30.0549	0.0610
5	45	PGF	2	3	44.9776	0.0249
5	82	PGF	3	4	81.9658	0.0380

Table 9: Fault classification, segment identification and location results for negative pole-to-ground faults.

Line	Fault distance [km]	Reported fault type	Reported sensor S_{up}	Reported sensor S_{dn}	Reported fault location [km]	Fault location error [%]
1	12	NGF	1	2	12.1413	0.0785
1	30.5	NGF	2	3	30.5261	0.0145
1	85	NGF	3	4	84.7860	-0.1189
1	137	NGF	5	6	137.1737	0.0965
1	163	NGF	6	7	162.9978	-0.0012
2	9	NGF	1	2	8.9238	-0.0635
2	31	NGF	2	3	31.0126	0.0105
2	68.2	NGF	3	4	68.1748	-0.0210
2	100	NGF	4	5	100.9580	0.7983
2	117	NGF	4	5	116.9158	-0.0702
3	18.8	NGF	1	2	18.7910	-0.0030
3	31	NGF	2	3	31.0510	0.0170
3	68.2	NGF	3	4	68.1313	-0.0229
3	155.5	NGF	6	7	155.7169	0.0723
3	238.9	NGF	8	9	238.5997	-0.1001
3	277.7	NGF	10	11	277.6160	-0.0280
3	297.5	NGF	10	11	297.8567	0.1189
4	5.5	NGF	1	2	5.7595	0.1730
4	66.6	NGF	3	4	66.9315	0.2210
4	99	NGF	4	5	98.8760	-0.0827
4	123	NGF	5	6	123.1289	0.0859
4	148.8	NGF	5	6	148.6092	-0.1272
5	11.3	NGF	1	2	12.0974	0.8860
5	45	NGF	2	3	44.9199	-0.0890
5	66.6	NGF	3	4	66.7160	0.1289
5	72	NGF	3	4	71.9103	-0.0997

4.5. Impact of fault resistance R_f

In order to further scrutinise the response of the proposed fault location algorithm, the case studies presented in Tables 7, 8 and 9 have been repeated for different values of fault resistance R_f.

Table 10: Average errors for PPF, PGF and NGF and different fault resistance values.

R_f [Ω]	**0**	**25**	**50**	**100**	**200**	**500**
PPF	0.0797	0.0816	0.0820	0.0825	0.8026	0.0839
PGF	0.0987	0.1020	0.1020	0.1054	0.1055	0.1063
NGF	0.1357	0.1404	0.1411	0.1422	0.1452	0.1466

The numerical results in terms of average values of error are presented in Table 10. Consistently satisfactory results have been reported with no significant increase in the average error even for highly resistive faults when $R_f = 500\,\Omega$. It can be concluded that the proposed fault location scheme is relatively robust to highly resistive faults.

It should be noted that any difference in the accuracy between different types of fault does not originate to any electrical asymmetry in the system. Any mismatch in the results might be expected due to artificial noise in measurements (as explained in Section 4.1), signal processing and simulation time in conjunction with distance to fault.

4.6. Impact of Mother Wavelet Ψ and scaling factor α

In order to extend the response of the proposed fault location algorithm, the pole-to-pole case studies presented in Table 7 have been repeated for different mother wavelets Ψ and scaling factors α. The results presented in Table 11 show a variety of errors including minimum (Min.), maximum (Max.) and average (Avg.).

Table 11: Fault location errors for PPFs and for different values of scaling factor α and mother wavelets Ψ.

α	**4**			**8**			**10**			**12**			**16**			**32**			**64**		
Ψ	Min.	Max.	Avg.	Min.	Max.	Avg.	Min.	Max.	Avg.	Min.	Max.	Avg.	Min.	Max.	Avg.	Min.	Max.	Avg.	Min.	Max.	Avg.
Haar	0.0000	0.3642	0.0746	0.0000	0.3642	0.0632	0.0000	0.1997	0.0797	0.0000	0.1997	0.0577	0.0000	0.2886	0.0776	0.0028	0.8249	0.1329	0.0000	1.4980	0.2823
db1	0.0000	0.3642	0.0746	0.0000	0.3642	0.0632	0.0000	0.1997	0.0522	0.0000	0.1997	0.0577	0.0000	0.2886	0.0775	0.0028	0.8249	0.1329	0.0000	1.4980	0.2823
db2	0.0000	2.500	0.4720	0.0000	1.4990	0.0300	0.0000	1.7020	0.0274	0.1658	4.8334	2.5190	0.0000	1.8320	0.4587	0.0000	2.7780	0.5342	0.1666	4.8329	2.5190
db3	0.0000	3.7430	0.2634	0.0000	4.9420	2.2620	0.1662	4.8330	2.5190	0.1665	4.8330	2.5190	0.0767	4.9490	2.5450	0.1667	4.8331	2.5190	0.0112	6.0940	2.5410
sym1	0.0000	0.3642	0.0746	0.0000	0.3642	0.0633	0.0000	0.1997	0.0522	0.0000	0.1997	0.0577	0.0000	0.2886	0.0776	0.0028	0.8249	0.1329	0.0000	1.4980	0.2823
sym2	0.0000	2.5000	0.4720	0.0000	1.4990	0.0300	0.0000	1.7020	0.0274	0.1667	4.8330	2.5190	0.0000	1.8320	0.4587	0.0000	2.7780	0.5342	0.1667	4.8330	2.5190
sym3	0.1669	4.8332	2.5190	0.0000	5.200	1.4180	0.1661	4.8329	2.5190	0.1667	4.8332	2.519	0.0261	5.4510	2.5920	0.1671	4.8331	2.5190	0.0107	5.4740	2.5420
sym4	0.0000	1.4130	0.1450	0.1667	4.8330	2.5190	0.0000	2.0090	0.1062	0.1667	4.8330	2.519	0.0000	5.2780	1.5720	0.1667	4.8328	2.5190	0.1257	4.8740	2.5180
coif1	0.1667	4.8330	2.5190	0.0000	1.5740	0.0645	0.0000	2.3360	0.3758	0.0000	2.5470	0.5144	0.0056	2.4310	0.6078	0.1670	4.7930	2.6870	0.0255	8.4790	2.7730
coif2	0.1669	4.8330	2.5190	0.1667	4.8330	2.5190	0.1667	4.8330	2.5190	0.1659	4.8330	2.5190	0.1667	4.8327	2.5190	0.0000	4.7200	2.05000	0.1433	4.8570	2.5150

The shortcoming of such thorough study is that for the proposed fault location algorithm Haar, db1 and db2 mother wavelets with a scaling factor of (or around) $\alpha = 10$ are the best compromises between minimum, maximum and average error.

4.7. Impact of Transmission Line Loading

In the interest of assessing the performance of the proposed scheme under the influence of different DC line load currents, the case studies described in Section 4.4 (whose corresponding numerical results are included in Tables 7, 8 and 9) have been repeated. In order to achieve different load conditions on the transmission lines, power exchange of the converters has been changed. In particular, as presented in Table 12, four different scenarios have been considered (for reference, it should be noted that Scenario II includes the results presented previously in Section 4.4).

Table 12: Active power set-points enabling different loading conditions of transmission lines.

Converter	**Scenario**			
	I	**II**	**III**	**IV**
MMC_1	V_{dc} control			
MMC_2	-0.40 GW	-0.80 GW	-1.20 GW	-1.6 GW
MMC_3	-0.35 GW	-0.70 GW	-1.05 GW	-1.4 GW
MMC_4	+0.25 GW	+0.50 GW	+0.75 GW	+1.0 GW
MMC_5	+0.25 GW	+0.50 GW	+0.75 GW	+1.0 GW

Positive values denote that power is imported into DC grid (i.e. converter operates in rectifier mode), while negative values indicate that power is exported to AC grid (i.e. converter operates in inverter mode). The control mode of MMC_1 has been set to 'DC voltage' and hence the power exchange is defined by the state of DC voltage (equivalent to slack bus in AC systems). All the remaining converters (i.e. MMC_2 to MMC_5) operate in 'active power' control mode with unity power factor, where the set-points of power are directly assigned.

Fault location results (in terms of average error) are presented separately for each line, loading scenario and fault type in Table 13. By observing the resulting fault location values, it can be observed that the accuracy is hardly affected by the loading conditions of transmission lines. Taking as reference Scenario II, the deviation of fault location values hovers randomly around $+0.53\ \%$ and $-0.65\ \%$.

Such imperceptible deviation does not emanate from different loading conditions of transmission lines, but it is rather a result of the random and artificial white noise added in the measurements. This is due the fact that the distance estimation of the proposed scheme depends on the time characteristics of current

Table 13: Fault location results for different loading conditions of transmission lines.

Scenario	Line	Average error [%]		
		PPF	PGF	NGF
I	1	0.0910	0.0966	0.0621
	2	0.1079	0.1090	0.1916
	3	0.0571	0.0972	0.0515
	4	0.0898	0.1176	0.1386
	5	0.0420	0.0677	0.3024
II	1	0.0909	0.0970	0.0619
	2	0.1079	0.1085	0.1927
	3	0.0573	0.0976	0.0517
	4	0.0896	0.1170	0.1380
	5	0.0422	0.0677	0.3009
III	1	0.0914	0.0964	0.0622
	2	0.1073	0.1088	0.1918
	3	0.0576	0.0974	0.0518
	4	0.0896	0.1175	0.1385
	5	0.0421	0.0675	0.3014
IV	1	0.0907	0.097	0.0618
	2	0.1080	0.1086	0.1921
	3	0.0575	0.0981	0.0518
	4	0.0897	0.1166	0.1377
	5	0.0420	0.068	0.3016

travelling waves (as also expressed by equations 6, 7 and 8), and not on the amplitude of DC current. Such time characteristics are not affected by the increasing or decreasing amplitude of DC current, and hence the proposed scheme is robust against different loading conditions of transmission lines.

4.8. Investigation of Excessive Noise

In the interest of investigating the performance of the proposed fault location method under the influence of noise in current measurements, the studies presented in Section 4.4 have been repeated. In particular, DC current measurements have been contaminated with increasing artificial noise of specific Noise-to-Signal-Ratio (NSR), starting from noise-less signal (i.e. infinite NSR) until 20 dB.

The resulting accuracy of the fault location estimation is presented in Table 14. It can be observed that lower dB values (corresponding to higher level of noise), have inescapably a negative effect on the accuracy. However, the resulting error increases by a factor in the range of $1.7\ \%$ for the NSR reaching 20 dB, which can be considered relatively low. Consequently, it can be concluded that the proposed fault location scheme is relatively robust to excessive noise.

Table 14: Fault location results for increasing values of noise.

SNR [dB]	Line	Average Error [%]			SNR [dB]	Line	Average Error [%]		
		PPF	PGF	NGF			PPF	PGF	NGF
	1	0.0909	0.097	0.0619		1	0.0912	0.0975	0.0621
	2	0.1079	0.1085	0.1927		2	0.1082	0.109	0.1934
∞	3	0.0573	0.0976	0.0517	50	3	0.0576	0.098	0.0519
	4	0.0896	0.117	0.1380		4	0.0899	0.1175	0.1385
	5	0.0422	0.0677	0.3009		5	0.0423	0.068	0.3021
	1	0.0908	0.097	0.0619		1	0.0914	0.0976	0.0623
	2	0.1078	0.1085	0.1928		2	0.1085	0.1092	0.1939
80	3	0.0573	0.0976	0.0517	40	3	0.0576	0.0981	0.052
	4	0.0897	0.117	0.1380		4	0.0901	0.1176	0.1387
	5	0.0422	0.0677	0.3009		5	0.0424	0.0681	0.3023
	1	0.0912	0.0971	0.0621		1	0.0912	0.0973	0.0622
	2	0.1082	0.1087	0.1934		2	0.1083	0.109	0.1934
70	3	0.0574	0.098	0.0518	30	3	0.0576	0.0983	0.0521
	4	0.0897	0.1174	0.1383		4	0.0902	0.1176	0.1391
	5	0.0423	0.0679	0.3015		5	0.0424	0.068	0.302
	1	0.0911	0.0972	0.0621		1	0.0924	0.098	0.0629
	2	0.1082	0.1088	0.1933		2	0.1096	0.11	0.1948
60	3	0.0575	0.0979	0.0518	20	3	0.058	0.0987	0.0523
	4	0.0898	0.1174	0.1384		4	0.0911	0.1182	0.1402
	5	0.0423	0.0678	0.3021		5	0.0429	0.0684	0.3052

The reason behind the immunity to noise of the proposed scheme, originates from the fact that DC current measurements are filtered prior to any other signal processing function. This is illustrated in Figure 6 in 'signal conditioning' block, which is also analysed in Appendix II and most significantly, proved experimentally in Section 5.3. Moreover, as discussed previously, the pattern recognition approach aids to the reduction of fault location errors arising from low sampling frequency and expectantly from excessive noise.

4.9. Impact of HVDC Protection and Control Schemes

When a fault occurs on transmission lines, voltage and current travelling waves are generated at the fault point and start propagating towards line terminals. Until such waves have arrived at line terminals, the fault has no impact as it has not been 'seen' by the converters or any other protection and control equipment. Most significantly, any device installed at line terminals, usually takes a few ms (after the first wave has arrived) to initiate any action. Such actions might result in fault current interruption [33, 34] or continuous operation [35, 36] with reduced voltage and/or current. However, until such actions take effect

on the system, voltages and currents are not affected (i.e. the system operates under its natural response) and hence there are available recorded data. The time range of such data, accounts for a few to several ms (i.e. in the range of 2 ms to 20 ms). It should be also highlighted that any protection and control equipment is expected to affect the magnitude of voltage and current. However, the arrival time of travelling waves (which is utilised in the proposed method) cannot be affected, as it is predominantly determined by the line characteristics and distance to fault. Taking into account all the above-mentioned facets, and also the fact that the proposed method requires only the first current travelling wave for fault distance calculation, the accuracy of proposed should not be affected at by any protection and control equipment.

4.10. Effect of Synchronisation Errors

Time precision of synchronised measurements are one of the key players to the accuracy of two-ended fault location techniques. Any time deviation could lead to large fault location errors, and hence reduce the accuracy of fault distance estimation [37]. In this part of the paper, times synchronisation errors and their impact on the fault location accuracy are investigated.

It should be emphasized here that the optical sensing arrangement utilised in the proposed scheme, scans all the distributed sensors from a single point, where one common trigger device is used. Consequently, time-synchronisation of measurements is enabled and ensured without the need of external clock (e.g. GPS) and communication links. In the proposed current sensing scheme, two major cases could lead to time synchronisation errors. The first one is related to the malfunction of sensors interrogator clock at the acquisition point. The latter one could arise from any disturbance at the sensor's and interrogator's point or due to any jitter within the optical fibre.

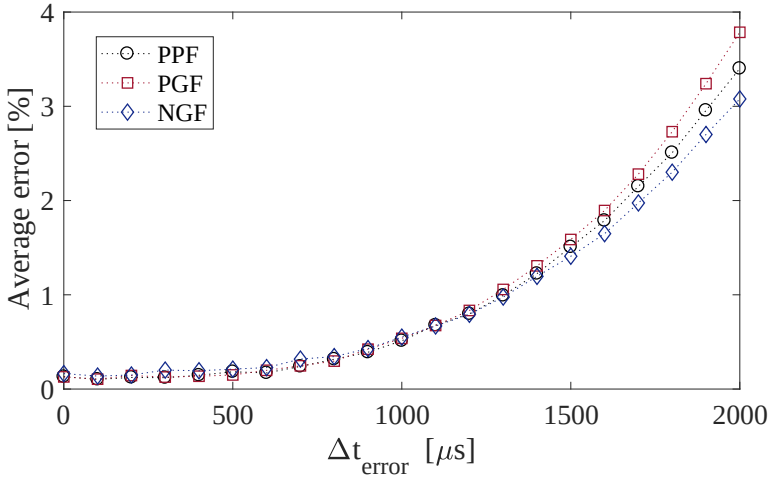

Figure 9: Impact of synchronisation error Δt_{error} to fault location accuracy.

In order to assess the impact of synchronisation error to the accuracy of the proposed fault location scheme, the studies presented in Section 4.4 have been repeated, integrating artificial synchronisation error Δt_{error}. The studies have been carried out separately for each type of fault and considered synchronisation errors of up to $2000\ \mu s$ (corresponding to deviation of 10 samples at 5 kHz). The resulting accuracy of the proposed scheme is presented in terms of average error in Figure 9. The outcome of such thorough study revealed that the proposed scheme can maintain the fault location error below $1\ \%$, for synchronisation errors rising up to $1250\ \mu s$. According to relevant technical literature [37, 38, 39], and considering low sampling rates in conjunction with the relatively large synchronisation errors, the results can be appraised quite efficient. As also discussed in Section 3.3, the utilisation of pattern recognition can lead to the reduction of fault location errors arising from low sampling rates, and apparently can retain the fault location errors within low limits, in the case of prolonged delays.

On the contrary, when greater values of synchronisation errors (i.e. $\Delta t \in [1250, 2000]\ \mu s$) were considered, the average error has been increased of up to $4\ \%$, and hence the accuracy has been diminished. It should be also highlighted that regardless the achieved accuracy, the faulted segment identification stage has operated correctly at $100\ \%$ of the cases.

5. Optical Sensing Technology

This section presents a set of experimental tests which verify the practical feasibility of DC current measurements. A similar experimental arrangement has been previously developed by the authors and has been used in [11] to enable distributed DC current measurements for high speed differential protection in HVDC networks. In recognition of space restrictions the theoretical analysis of the optically-based DC current measurements is not presented thoroughly. For an in-depth analysis and further technical specifications, the literature in [11, 40, 41] may be consulted.

5.1. Hybrid FBG-based voltage and current sensors

For the purposes of validating the feasibility of the distributed DC current sensing scheme, four FBGs inscribed in polyimide coated fibers, having a bandwidth of 0.3 nm, peak wavelengths at 1539.60, 1551.56, 1554.72 and 1557.38 nm (see Figure 10) and a length of 7 mm, have been utilised.

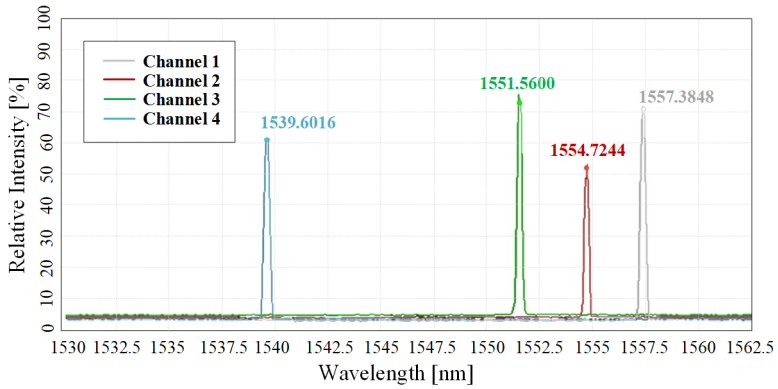

Figure 10: FBGs spectra.

For the construction of a hybrid low voltage sensor, a 9 mm voltage stack has been used (P-883.11 PICMA[42]) and is shown in Figure 11. The relative elongation $\Delta l/l$ induced by an external electric field is given by equation 15.

$$\epsilon = d_{33}E = d_{33}\frac{V}{l} \tag{15}$$

where, d_{33} is the longitudinal piezoelectric charge constant; E is the electric field; V is the voltage applied across the piezoelectric material; and l is the length of the material [43].

Consequently, an applied voltage across the stack will generate a mechanical strain which is exerted on the FBG. This will result in a corresponding shift in its peak wavelength; and thus, the peak wavelength shift can be calibrated in terms of voltage [43].

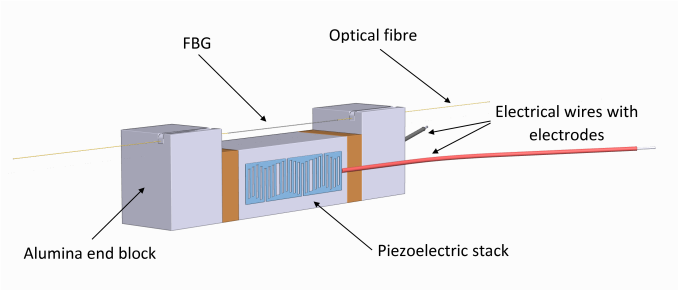

Figure 11: Hybrid FBG-based voltage sensor.

Ideally, by replacing a piezoelectric component with a magnetostrictive transducer, a sensor capable of measuring DC current can be constructed [44].

5.2. Experimental Setup

The diagram of the experimental setup used for the validation of the proposed scheme and the actual arrangements are depicted in Figures 12 and 13 respectively. In this setup, four sensors have been utilised assuming they are spaced equally across a 300 km HVDC transmission line (Line 3 in the MTDC network shown in Figure 7).

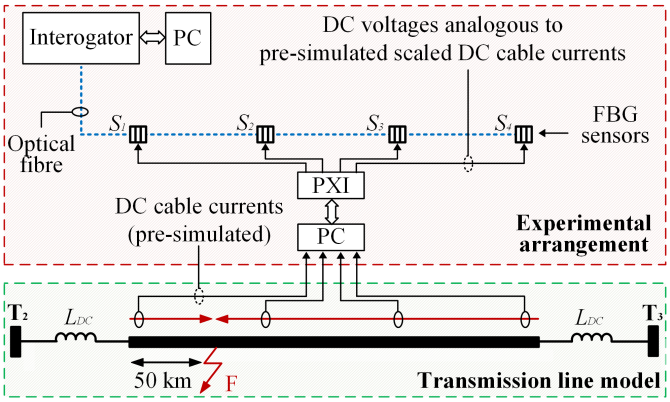

Figure 12: Schematic of experimental setup. Fault occurrence is shown between sensors S2 and S3 at 150 km.

Pre-simulated DC fault currents at four sensing locations along the transmission line were used to generate replica voltage waveforms (produced from a multi-function data acquisition card). Such scaled-down voltage traces (which correspond to the scaled DC line currents) were physically input to the optical sensors and an optical interrogator has been used for data sampling, and then, the data were stored on a PC for post-analysis by the fault location algorithm.

Due to hardware limitations and to further simplify the experimental circuitry, four FBG optical voltage sensors were used directly.

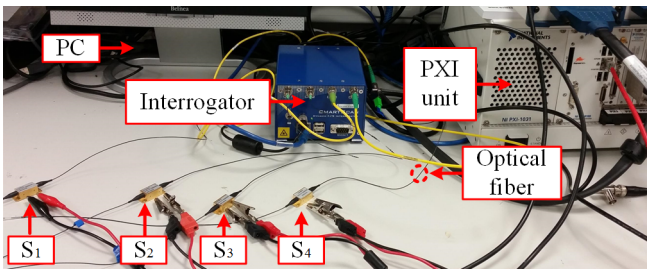

Figure 13: Laboratory experimental setup.

The FBGs were connected (optically) to an interrogator offering a scanning frequency of 2.5 kHz (spectral range: 1528-1568 nm). To futher increase the scanning frequency, maximum wavelength range of the device was narrowed to 1538-1558 nm. Therefore, the optical signals reflected from the sensors were acquired at a frequency of 5 kHz. Prior to low-voltage test, sensors were characterized and calibrated.

5.3. Experimental Results

The measured response of the optical sensors to a fault at 300 km line occurring at 50 km (see Figure 12) is shown in Figure 14.

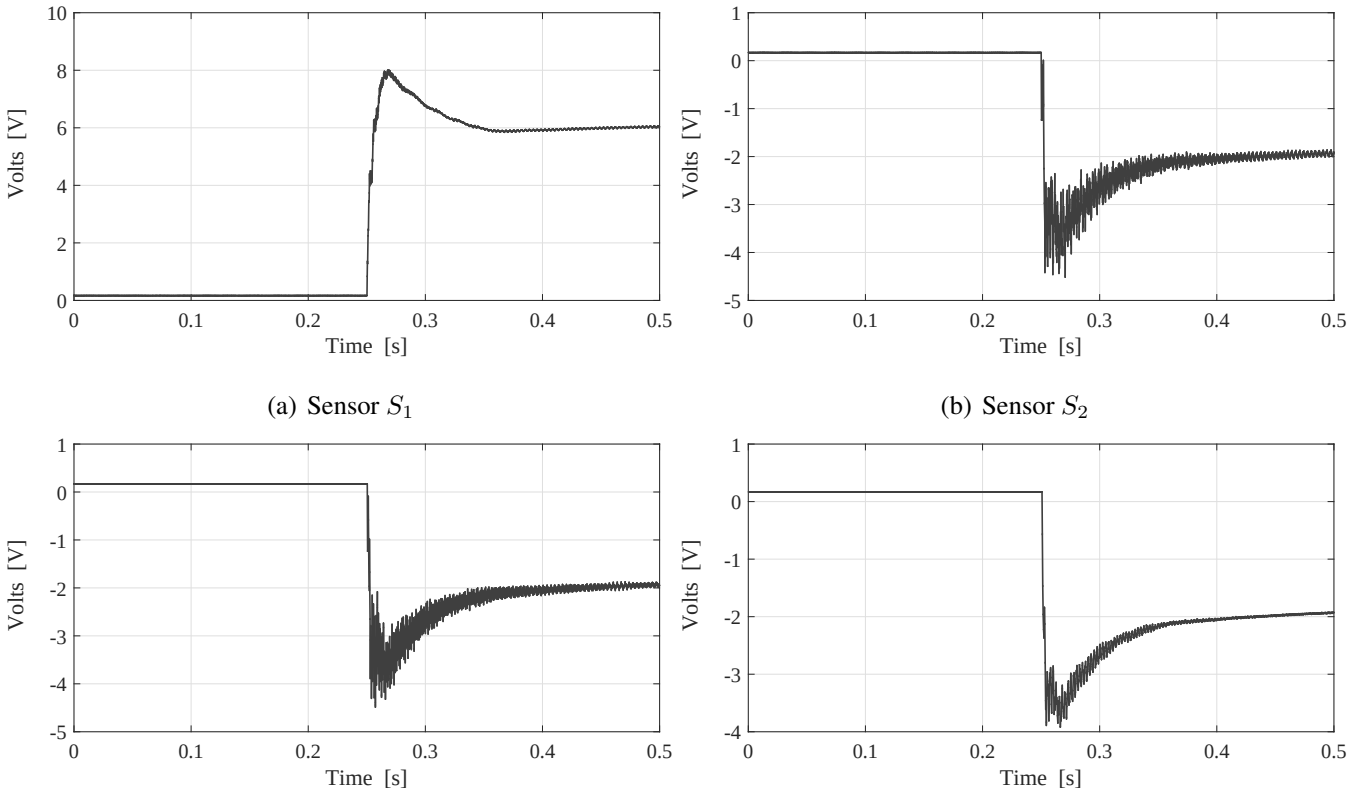

(a) Sensor S_1 (b) Sensor S_2

(c) Sensor S_3 (d) Sensor S_4

Figure 14: Voltage traces representing DC line currents at four sensing locations as per Figure 12.

The recorded DC voltages are scaled-down replicas of the DC line currents which were pre-simulated and physically generated in real-time using a data acquisition card.

These voltage traces were physically input to the FBG optical sensors. The sampled data obtained from the optical interrogation system was stored on a PC for processing as illustrated in Figure 15. The depicted traces represent the reflected Bragg Wavelength $\Delta\lambda_B$, individually for each sensor. Due to mechanical inertia of the sensors and other environmental conditions, (e.g. temperature) the raw measured response (black solid line) of the sensor contains a significant level of noise.

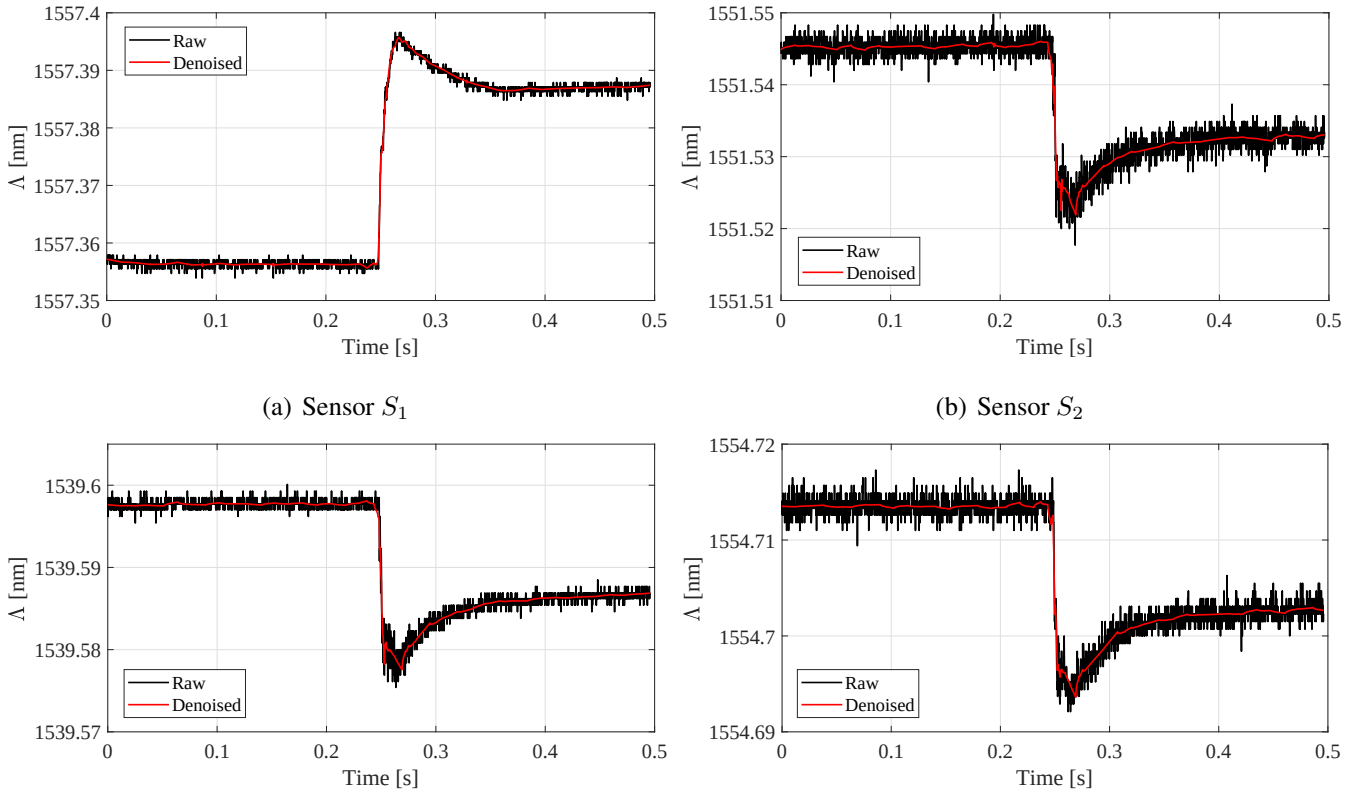

(a) Sensor S_1

(b) Sensor S_2

(c) Sensor S_3

(d) Sensor S_4

Figure 15: Sensors response to DC voltage traces depicted in Figure 14.

For this reason, the measurements have been filtered by using Discrete Wavele multi-resolution analysis (see Appendix II for further explanation). In particular, the measurements have been decomposed and reconstructed using a six-level tree analysis and fixed threshold denoising. The denoised signals are also illustrated alongside the raw measurements in Figure 15. It is evident that the denoised signals contain less noise and can be used with much more confidence for fault location applications.

The inverted function was used again to normalise the DC voltage in terms of shifted Bragg Wavelength $\Delta\lambda_B$. The resulting waveforms of wavelength-to-voltage conversion are individually illustrated in Figure

16 for each sensor. It is evident that these traces are of great resemblance with the originally-simulated (see Figure 14).

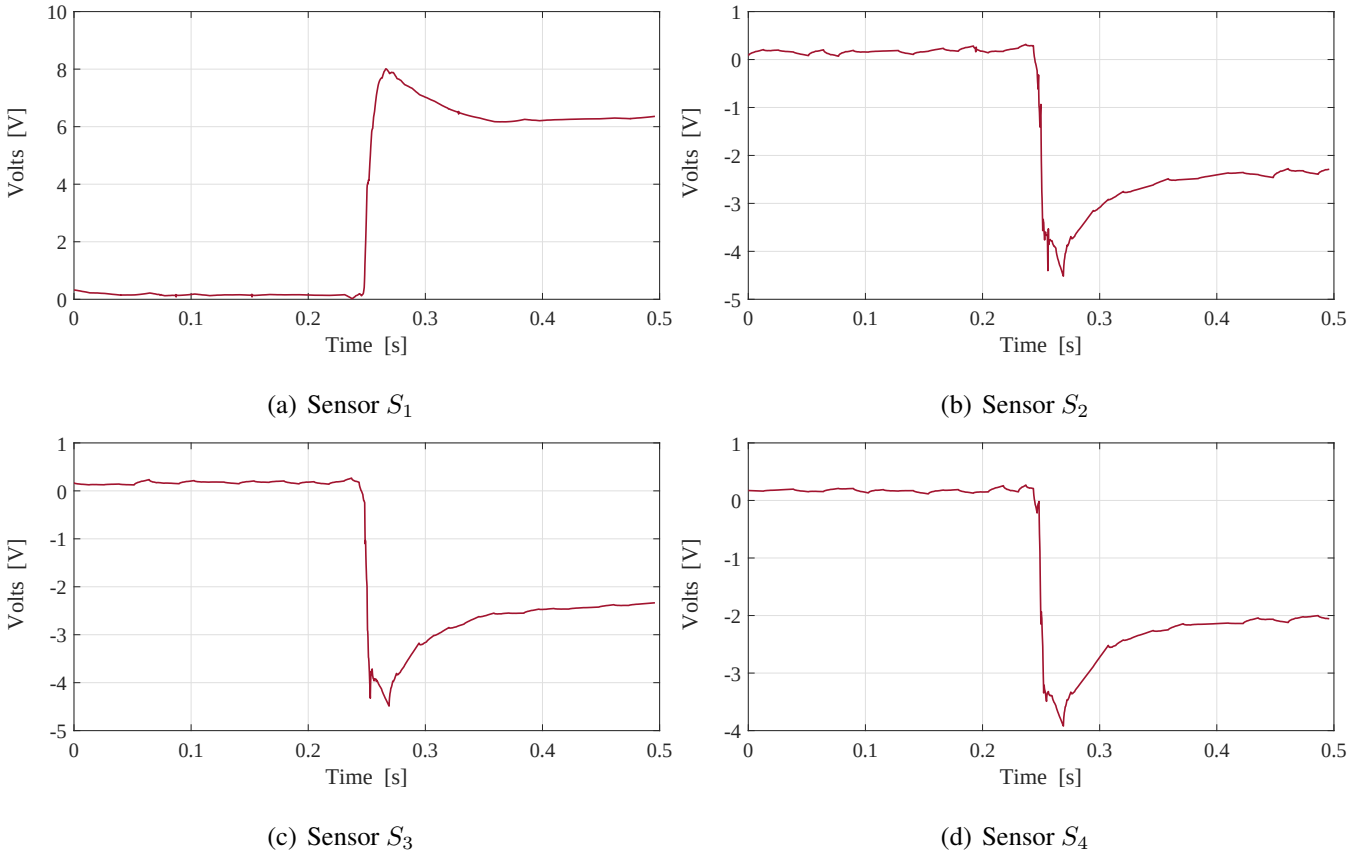

(a) Sensor S_1 (b) Sensor S_2

(c) Sensor S_3 (d) Sensor S_4

Figure 16: Normalised DC voltages corresponding to shifted Bragg Wavelengths $\Delta\lambda_B$.

The normalised DC voltages (corresponding to DC currents) can form an input on a platform for post-processing. Consequently, a fault location algorithm (or any other algorithm or function) can be realised.

5.4. Technical and Economical Merits

Distributed sensing in power systems is an advanced, cutting-edge technology (with numerous operational, technical and economic benefits) which aims to accelerate power system protection and control applications [11, 41, 45, 46, 47, 48]. The key technical and economical merits of the utilised distributed sensing technology (compared to conventional electrical and other optical methods), arise from the fact that the sensors are completely passive and require no power. Moreover, there is no need of other signal processing and communication equipment (i.e. GPS, micro-controllers, etc.) at the location of the sensors (i.e. sensors are interrogated from a single acquisition point, where measurements are also time-stamped). These technical merits will enable reduction in the hardware and infrastructure needs (i.e. communications, low voltage power supplies, decoders/encoders, etc.) required for wide-area monitoring. It should be also noted

that over the past decade the cost of FBG sensors has been reduced substantially, leading to the realization of high performance and cheap transducers.

Overall, due to the extensibility and centralised nature of the sensing technology, the capability of distributed sensing can be technically beneficial, while can ultimately result in reduction of capital and operational costs.

6. Conclusions

In this paper a new fault location scheme for MTDC grids has been proposed which utilises the principle of distributed optical sensing, travelling waves and a machine learning approach. It has been found that the proposed scheme can accurately classify the fault type including pole-to-pole, positive pole-to-ground and negative pole-to-ground faults. It has also been demonstrated that the fault location can be calculated with increased accuracy. Specifically, it has been found that the minimum, maximum and average error for PPFs was 0.0000 %, 0.1997 % and 0.0797 %, respectively; for PFGs those errors correspond to 0.0100 %, 0.2310 % and 0.0987 %; and for NGF to 0.0012 %, 0.8860 % and 0.1357 %, respectively. The scheme has also demonstrated to be accurate even with highly resistive faults with values of up to 500 Ω. A sensitivity analysis on different mother wavelets Ψ and scaling factors α revealed that for the proposed fault location algorithm, Haar, db1 and db2 mother wavelets with a scaling factor of (or around) $\alpha = 10$ are the best compromises between minimum, maximum and average error. The proposed scheme has been also found to be robust against different loading conditions of transmission lines and excessive noise contained in current measurements. The effect of time-synchornisation errors has been also investigated, and the scheme has been found to maintain accuracy below 1 % for time delays rising up tp 1250 μs. A series of experimental test sets demonstrated that the distributed optical current sensing scheme is practically feasible. Consequently there is confidence with regards the practical implementation of the scheme. The merits of wavelet transform have been demonstrated which include wave detection and signal denoising. A few considerations including the impact of HVDC control systems, the technical and economic merits of distributing sensing have been also discussed.

Appendix I - Wavelet Transform

The wavelet transform of a function $v(t)$ can be expressed as the integral of the product of $v(t)$ and the daughter wavelet $\Psi^*_{a,b}(t)$ as presented in equation 16.

$$WT_{\psi(\alpha,b)}v(t) = \int_{-\infty}^{+\infty} v(t) \underbrace{\frac{1}{\sqrt{\alpha}}\Psi\left(\frac{t-b}{a}\right)}_{\text{daughter wavelet } \Psi^*_{a,b}(t)} dt \tag{16}$$

The daughter wavelet $\Psi^*_{a,b}(t)$ is a scaled and shifted version of the mother wavelet $\Psi_{a,b}(t)$. Scaling is implemented by α, which is the binary dilation (also known as scaling factor) and shifted by b, which is the binary position (also known as shifting or translation). If the function $v(t)$ and mother wavelet $\Psi_{a,b}(t)$ are real functions, then the resulting $WT_{\psi(\alpha,b)}v(t)$ is also a real function. In any other case mother wavelet $\Psi_{a,b}(t)$ and the resulting $WT_{\psi(\alpha,b)}v(t)$ are complex functions.

Wavelet transform can be distinguished in two categories, namely Continuous Wavelet Transform (CWT) and Discrete Wavelet Transform (DWT). The difference lies upon the resolution of binary dilation α and binary position b. In DWT, they move discretely in dyadic blocks. Specifically, α and b, can only take values of the power of two as expressed in equation (17).

$$\left.\begin{aligned} \alpha_j &= 2^j,\ (\alpha_0 = 2^0 = 1, \alpha_1 = 2^1 = 2, ...) \\ b_j &= 2^j N,\ (b_0 = 2^j 0 = 0, b_1 = 2^j 1 = 2^j, ...) \end{aligned}\right\} \tag{17}$$

where, j is the level of decomposition and N is the sample index.

Consequently, the CWT described in equation 16 results in the following discrete form:

$$WT_{\psi(2^j,b)}v(t) = \int_{-\infty}^{+\infty} v(t)\frac{1}{\sqrt{2^j}}\Psi\left(\frac{t-2^jN}{2^j}\right) dt \tag{18}$$

The selection between CWT and DWT is a trade-off between time accuracy of the wave detection, and processing resources and their associated time delays [49]. In the case of CWT, the daughter wavelet can be positioned smoothly over the signal, and hence, the accuracy of the wave time detection is better than DWT techniques. This is the reason that CWT is preferred for fault location applications [14], where the computational time is not crucial. However, DWT is computationally more efficient [49], which enables faster wave detection. As a result, DWT is considered more suitable for power system protection applications [50].

Appendix II - Wavelet Multi-resolution Analysis

When DWT is applied to a discrete signal $v(n)$, the signal can be decomposed into high-frequency detailed and low-frequency approximation coefficients as shown in equations 19 and 20 respectively.

$$W_{2^j}v(n) = \sum_k g_k A_{2^{j-1}}v(n - 2^{j-1}k) \tag{19}$$

$$A_{2^j}v(n) = \sum_k h_k A_{2^{j-1}}v(n - 2^{j-1}k) \tag{20}$$

where, g_k is the high-pass filter coefficients; h_k is the low-pass filter coefficients; and A_{2^0} is the initial signal.

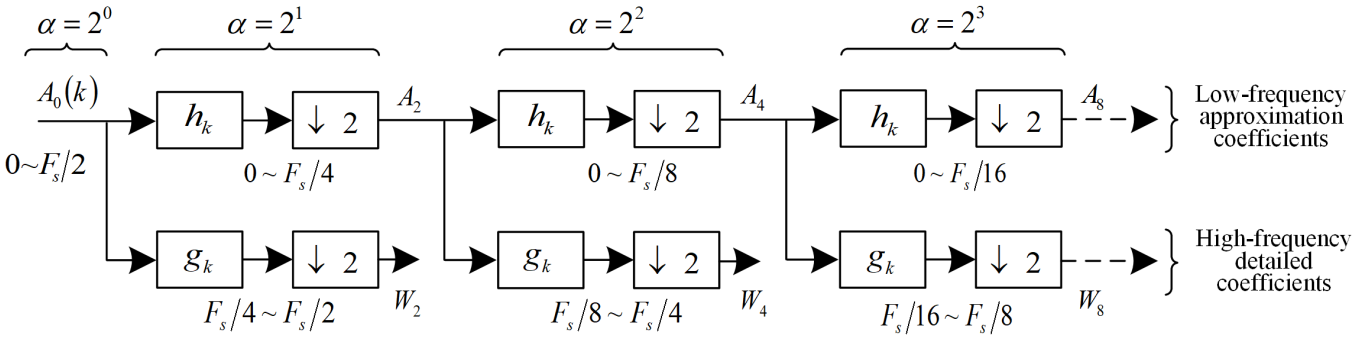

Figure 17: Decomposition structure for multi-resolution analysis based on filter banks.

Taking into account that signal $v(n)$ has a sampling frequency F_s, it contains components in the frequency spectrum $0 \sim F_s/2$ as per Nyquist Theorem. As shown in Figure 17, DWT decomposes the signal into different frequency bands, and therefore, *'multiresolution'* analysis is achieved [51]. The frequency bandwidth of high-frequency detailed and low-frequency approximation coefficients for each decomposition level are shown in equations 21 and 22, respectively.

$$f_{band-high} = \frac{F_s}{2 \cdot 2^j} \sim \frac{F_s}{2 \cdot 2^{j-1}} \tag{21}$$

$$f_{band-low} = 0 \sim \frac{F_s}{2 \cdot 2^j} \tag{22}$$

It is therefore evident that according to the frequency band of interest, the corresponding scaling factor may be selected.

The multi-resolution decomposition analysis depicted in Figure 17 can be implemented in a bi-directional manner. This means that a signal can be decomposed to a desired number of levels and then re-constructed using only the coefficients of interest. Consequently, the two-way wavelet-based multi-resolution analysis can be used for the purpose of selective filtering.

Acknowledgements

The present article outlines the results of a collaborative work conducted between University of Strathclyde, Glasgow, UK and Tsinghua University, Beijing, China. This work was supported in part by the GE Solutions Ltd., in part by the Innovate U.K. (TSB Project 102594), in part by the European Metrology Research Programme (EMRP)-ENG61, and in part by the National Key Research and Development Plan of China (Grant No. 2016YFB0900600). The EMRP is jointly funded by the EMRP participating countries within EURAMET and the European Union.

[1] D. Tzelepis, A. O. Rousis, A. Dysko, C. Booth, G. Strbac, A new fault-ride-through strategy for MTDC networks incorporating wind farms and modular multi-level converters, Electrical Power and Energy Systems 92 (2017) 104–113.

[2] R. Zeng, L. Xu, L. Yao, S. J. Finney, Y. Wang, Hybrid HVDC for integrating wind farms with special consideration on commutation failure, IEEE Transactions on Power Delivery 31 (2) (2016) 789–797.

[3] W. Leterme, P. Tielens, S. D. Boeck, D. V. Hertem, Overview of grounding and configuration options for meshed HVDC grids, IEEE Transactions on Power Delivery 29 (6) (2014) 2467–2475.

[4] A. Raza, X. Dianguo, L. Yuchao, S. Xunwen, B. W. Williams, C. Cecati, Coordinated operation and control of VSC based multiterminal high voltage DC transmission systems, IEEE Transactions on Sustainable Energy 7 (1) (2016) 364–373.

[5] R. Zeng, L. Xu, L. Yao, D. Morrow, Precharging and DC fault ride-through of hybrid MMC-based HVDC systems, IEEE Transactions on Power Delivery 30 (3) (2015) 1298–1306.

[6] V. Akhmatov, M. Callavik, C. Franck, S. Rye, T. Ahndorf, M. Bucher, H. Muller, F. Schettler, R. Wiget, Technical guidelines and prestandardization work for first HVDC grids, IEEE Transactions on Power Delivery 29 (1) (2014) 327–335.

[7] G. Tang, Z. He, H. Pang, X. Huang, X. p. Zhang, Basic topology and key devices of the five-terminal DC grid, CSEE Journal of Power and Energy Systems 1 (2) (2015) 22–35.

[8] N. R. Chaudhuri, B. Chaudhuri, R. Majumder, A. Yazdani, Multi-Terminal Direct-Current Grids - Modeling, Analysis, and Control, IEEE Press - Willey, 2014.

[9] D. Tzelepis, S. Ademi, D. Vozikis, A. Dysko, S. Subramanian, H. Ha, Impact of VSC converter topology on fault characteristics in HVDC transmission systems, in: IET 8th International Conference on Power Electronics Machines and Drives, 2016.

[10] E. Kontos, R. Pinto, S. Rodrigues, P. Bauer, Impact of HVDC transmission system topology on multiterminal DC network faults, IEEE Transactions on Power Delivery 30 (2) (2015) 844–852.

[11] D. Tzelepis, A. Dyko, G. Fusiek, J. Nelson, P. Niewczas, D. Vozikis, P. Orr, N. Gordon, C. D. Booth, Single-ended differential protection in mtdc networks using optical sensors, IEEE Transactions on Power Delivery 32 (3) (2017) 1605–1615.

[12] S. Azizi, M. Sanaye-Pasand, M. Abedini, A. Hasani, A traveling-wave-based methodology for wide-area fault location in multiterminal DC systems, IEEE Transactions on Power Delivery 29 (6) (2014) 2552–2560.

[13] M. Farshad, J. Sadeh, A novel fault-location method for HVDC transmission lines based on similarity measure of voltage signals, IEEE Transactions on Power Delivery 28 (4) (2013) 2483–2490.

[14] O. Nanayakkara, A. Rajapakse, R. Wachal, Location of DC line faults in conventional HVDC systems with segments of cables and overhead lines using terminal measurements, IEEE Transactions on Power Delivery 27 (1) (2012) 279–288.

[15] O. Nanayakkara, A. Rajapakse, R. Wachal, Traveling-wave-based line fault location in star-connected multiterminal HVDC systems, IEEE Transactions on Power Delivery 27 (4) (2012) 2286–2294.

[16] L. Yuansheng, W. Gang, L. Haifeng, Time-domain fault-location method on HVDC transmission lines under unsynchronized two-end measurement and uncertain line parameters, IEEE Transactions on Power Delivery 30 (3) (2015) 1031–1038.

[17] Z. you He, K. Liao, X. peng Li, S. Lin, J. wei Yang, R. kun Mai, Natural frequency-based line fault location in HVDC lines, IEEE Transactions on Power Delivery 29 (2) (2014) 851–859.

[18] J. Suonan, S. Gao, G. Song, Z. Jiao, X. Kang, A novel fault-location method for HVDC transmission lines, IEEE Transactions on Power Delivery 25 (2) (2010) 1203–1209.

[19] M. Bawart, M. Marzinotto, G. Mazzanti, Diagnosis and location of faults in submarine power cables, IEEE Electrical Insulation Magazine 32 (4) (2016) 24–37.

[20] G. Y. Kwon, C. K. Lee, G. S. Lee, Y. H. Lee, S. J. Chang, C. K. Jung, J. W. Kang, Y. J. Shin, Offline fault localization technique on HVDC submarine cable via time-frequency domain reflectometry, IEEE Transactions on Power Delivery 32 (3) (2017) 1626–1635.

[21] A. K. Pradhan, A. Routray, S. Pati, D. K. Pradhan, Wavelet fuzzy combined approach for fault classification of a series-compensated transmission line, IEEE Transactions on Power Delivery 19 (4) (2004) 1612–1618.

[22] R. Salat, S. Osowski, Accurate fault location in the power transmission line using support vector machine approach, IEEE Transactions on Power Systems 19 (2) (2004) 979–986.

[23] P. K. Dash, S. R. Samantaray, G. Panda, Fault classification and section identification of an advanced series-compensated transmission line using support vector machine, IEEE Transactions on Power Delivery 22 (1) (2007) 67–73.

[24] U. B. Parikh, B. Das, R. P. Maheshwari, Combined wavelet-svm technique for fault zone detection in a series compensated transmission line, IEEE Transactions on Power Delivery 23 (4) (2008) 1789–1794.

[25] H. Livani, C. Y. Evrenosoglu, A machine learning and wavelet-based fault location method for hybrid transmission lines, IEEE Transactions on Smart Grid 5 (1) (2014) 51–59.

[26] H. Livani, C. Y. Evrenosoglu, A single-ended fault location method for segmented HVDC transmission line, Electric Power Systems Research 107 (2014) 190–198.

[27] J. M. Johnson, A. Yadav, Complete protection scheme for fault detection, classification and location estimation in HVDC transmission lines using support vector machines, IET Science, Measurement Technology 11 (3) (2017) 279–287.

[28] C. Atkeson, A. Moore, S. Schaal, Artificial intelligence review 11 (1) (1997) 11–73.

[29] W. M.P, J. M.C., Kerner Smoothing - Chapman & Hall, 1995.

[30] EU, Twenties project - final report, Tech. rep. (Oct 2013).

[31] CIGRE, Guide for the development of models for HVDC converters in a HVDC grid, Tech. rep., Working Group:B4.57 (2014).

[32] S. Li, X. Wang, Z. Yao, T. Li, Z. Peng, Circulating current suppressing strategy for MMC-HVDC based on nonideal proportional resonant controllers under unbalanced grid conditions, IEEE Transactions on Power Electronics 30 (1) (2015) 387–397.

[33] M. Mobarrez, M. G. Kashani, S. Bhattacharya, A novel control approach for protection of multi-terminal VSC-based HVDC transmission system against DC faults, IEEE Transactions on Industry Applications 52 (5) (2016) 4108–4116.

[34] M. Bucher, C. Franck, Fault current interruption in multiterminal HVDC networks, IEEE Transactions on Power Delivery PP (99) (2015) 1–1.

[35] R. Li, L. Xu, L. Yao, B. W. Williams, Active control of DC fault currents in DC solid-state transformers during ride-through operation of multi-terminal HVDC systems, IEEE Transactions on Energy Conversion 31 (4) (2016) 1336–1346.

[36] R. Li, L. Xu, D. Holliday, F. Page, S. J. Finney, B. W. Williams, Continuous operation of radial multiterminal HVDC systems under DC fault, IEEE Transactions on Power Delivery 31 (1) (2016) 351–361.

[37] V. Terzija, G. Preston, V. Stanojevi, N. I. Elkalashy, M. Popov, Synchronized measurements-based algorithm for short transmission line fault analysis, IEEE Transactions on Smart Grid 6 (6) (2015) 2639–2648.

[38] M. Davoudi, J. SADEH, E. Kamyab, Transient-based fault location on three-terminal and tapped transmission lines not requiring line parameters, IEEE Transactions on Power Delivery PP (99) (2017) 1–1.

[39] M. Davoudi, J. Sadeh, E. Kamyab, Parameter-free fault location for transmission lines based on optimisation, IET Generation, Transmission Distribution 9 (11) (2015) 1061–1068.

[40] G. Fusiek, P. Niewczas, J. McDonald, Feasibility study of the application of optical voltage and current sensors and an arrayed waveguide grating for aero-electrical systems, Sensors and Actuators A: Physical 147 (1) (2008) 177–182.

[41] P. Orr, G. Fusiek, C. D. Booth, P. Niewczas, A. Dyko, F. Kawano, P. Beaumont, T. Nishida, Flexible protection architectures using distributed optical sensors, in: Developments in Power Systems Protection, 11th International Conference on, 2012, pp. 1–6.

[42] Corning-Inc., SMF-28® ultra optical fiber, `www.corning.com/media/worldwide/coc/documents/Fiber/SMF-28%20Ultra.pdf`, [25-10-2016].

[43] L. Dziuda, P. Niewczas, G. Fusiek, J. R. McDonald, Hybrid fiber optic voltage sensor for remote monitoring of electrical submersible pump motors, Optical Engineering 44 (6) (2005) 064401–064401–6.

[44] D. Reilly, A. J. Willshire, G. Fusiek, P. Niewczas, J. R. Mcdonald, M. Ieee, A Fiber-Bragg-Grating-Based Sensor for Simultaneous AC Current and Temperature Measurement, IEEE Sensors Journal 6 (6) (2006) 1539–1542.

[45] P. Orr, G. Fusiek, P. Niewczas, C. D. Booth, A. Dyko, F. Kawano, T. Nishida, P. Beaumont, Distributed photonic instrumentation for power system protection and control, IEEE Transactions on Instrumentation and Measurement 64 (1) (2015) 19–26.

[46] P. Orr, C. Booth, G. Fusiek, P. Niewczas, A. Dysko, F. Kawano, P. Beaumont, Distributed photonic instrumentation for smart grids, in: Applied Measurements for Power Systems,IEEE International Workshop on, 2013, pp. 63–67.

[47] G. Fusiek, P. Orr, P. Niewczas, Temperature-independent high-speed distributed voltage measurement using intensiometric FBG interrogation, in: IEEE International Instrumentation and Measurement Technology Conference, 2015, pp. 1430–1433.

[48] P. Orr, G. Fusiek, P. Niewczas, A. Dyko, C. Booth, F. Kawano, G. Baber, Distributed optical distance protection using FBG-based voltage and current transducers, 2011 IEEE Power and Energy Society General Meeting (2011) 1–5.

[49] F. Liang, B. Jeyasurya, Transmission line distance protection using wavelet transform algorithm, IEEE Transactions on Power Delivery 19 (2) (2004) 545–553.

[50] X. Dong, J. Wang, S. Shi, B. Wang, B. Dominik, M. Redefern, Traveling wave based single-phase-to-ground protection method for power distribution system, CSEE Journal of Power and Energy Systems 1 (2) (2015) 75–82.

[51] S. Mallat, W. L. Hwang, Singularity detection and processing with wavelets, IEEE Transactions on Information Theory 38 (2) (1992) 617–643.